Three-Dimensional Structure of Electroosmotic Flow over Heterogeneous Surfaces

David Erickson and Dongqing Li*

Department of Mechanical and Industrial Engineering, University of Toronto, 5 King's College Road, Toronto, Ontario, Canada, M5S 3G8

Received: December 15, 2002; In Final Form: August 20, 2003

Electroosmotic flow is widely used as a primary method of species transport in microscale biological and chemical analysis systems commonly referred to as labs-on-a-chip. In these systems, surface electrokinetic heterogeneity can be introduced either intentionally through micromanufacturing technology, such as microcontact printing, or unintentionally through, for example, bioparticle adhesion. In either case it is desirable to examine the influence of these surface heterogeneities on the electroosmotic flow structure. In this paper a numerical model based on a simultaneous solution to the Nernst−Planck, Poisson, and Navier−Stokes equations is used to examine the electroosmotically driven flow through a microchannel exhibiting a periodically repeating patchwise heterogeneous surface pattern. The simulations have revealed a distinct three-dimensional flow structure that, depending on the degree of heterogeneity, varies from a weak circulation perpendicular to the applied electric field to a fully circulatory flow system. In general the induced flow structure is found to penetrate into the bulk flow no deeper than the length scale of the heterogeneous patches. In addition the electrophoritic influence of the applied electric field on the net charge density in the double layer is shown to cause a significant deviation from the traditional Poisson−Boltzmann distribution. The overall effect of this double-layer rearrangement on the flow structure, however, is found to be negligible.

1. Introduction

Microfluidics can trace its roots back to the development of such devices as the gas chromatograph and the inkjet printer, but the majority of current research in the field is focused on the lab-on-a-chip concept of reducing benchtop instruments to chip-sized analytical devices. In the majority of these systems, electrokinetic means (i.e., electroosmotic flow, electrophoresis) are the preferred method of species transport, as they offer significant advantages over traditional pressure-driven flow. When a liquid comes into contact with a solid, the formation of an interfacial charge causes a rearrangement of the local free ions in the liquid so as to produce a thin region of nonzero net charge density, commonly referred to as the electrical double layer (EDL), near the interface. The application of an external electric field results in a net body force on the free ions within the EDL inducing a bulk fluid motion called electroosmotic flow. The ability to control the rate and direction of flow through creative ways of dynamically manipulating the applied electric field has given researchers the means to focus,[1] dispense,[2] and transport[3−5] highly concentrated nanoliter-sized samples intended for separation or further chemical analysis. Inevitably these basic techniques have been extended, yielding creative channel and voltage arrangements to enhance species mixing[6] or to perform multistage analysis on a chip.[7−9] Although long recognized as a potential problem leading to irregular flow patterns and nonuniform species transport, only recently have authors begun to investigate the potential benefits that the presence of surface electrokinetic heterogeneity (nonuniform surface ζ-potential or charge density) may have to offer.

The earliest interest in the electrokinetics of heterogeneous surfaces involved pressure-driven flows and the streaming potential technique to monitor the dynamic or static adsorption of proteins,[10−13] surface-active substances,[14] and other colloidal or nanosized particles.[15,16] In this technique the surface's electrokinetic properties are altered by introducing a heterogeneous region, for example due to protein adsorption, which has a different ζ-potential than the original surface. The introduction of this heterogeneous region induces a change in the surface's average ζ-potential, which is monitored via a streaming potential measurement, and related back to the degree of surface coverage. To model this effect, a few analytical and numerical models have been proposed[15−18] which were primarily concerned with double-layer charge transport in the presence of this pressure-driven flow field. Only recently has a comprehensive examination of the complete three-dimensional pressure-driven flow field been performed,[19] revealing a number of interesting effects such as the presence of weak circulation regions perpendicular to the main flow axis.

As mentioned above, of greater interest to microfluidic applications is the influence of surface heterogeneity on an electroosmotically driven flow field. Ajdari,[20−22] Anderson,[23] and Ghosal[24] conducted pioneering studies examining these effects. In Ajdari's works it was predicted that the presence of surface heterogeneity could result in regions of bulk flow circulation, referred to as "tumbling" regions. This behavior was later observed in slit microchannels experimentally by Stroock et al.,[25] who found excellent agreement with their flow model. Long et al.[26] also developed an analytical model for an isolated heterogeneous spot in a flat plate or capillary geometry. In another study Herr et al.[27] used a caged dye velocometry technique to study electroosmotic flow in a capillary and observed significant deviations from the classical plug type velocity profile in the presence of heterogeneous surface properties, an effect that was predicted by Keely et al.[28] In another clever application Johnson et al.[29] used a UV excimer

* To whom correspondence should be addressed. E-mail: dli@mie.utoronto.ca.

10.1021/jp027724c CCC: $25.00
Published on Web 10/10/2003

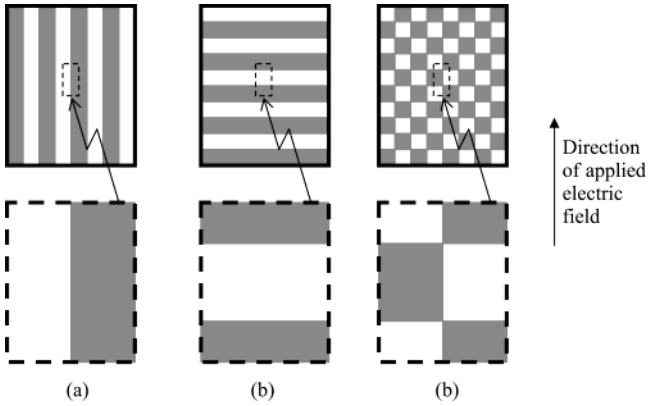

Figure 1. Periodic surface patterns: (a) lengthwise strips, (b) crosswise strips, (c) patchwise pattern. Dark regions represent heterogeneous patches, light regions are the homogeneous surface. In each case the percent heterogeneous coverage is 50%.

laser to introduce surface heterogeneity to the side wall of a polymeric microchannel and demonstrated how this could reduce sample band broadening around turns. Recently the use of surface heterogeneity to increase the mixing efficiency of a T-shaped micromixer has also been proposed.[30]

To fully understand and potentially exploit this phenomenon, the details of the complex three-dimensional electroosmotic flow structure in the presence of surface heterogeneity has to be studied. The purpose of this study is to investigate the flow in such a system using a specially developed microfluidics-based finite element code. The numerical model used here is based on a simultaneous solution to the Nernst−Planck, Poisson, and Navier−Stokes equations, which also allows us to shed the Poisson−Boltzmann double-layer distribution assumption and to adopt a more general approach. In the following sections the analytical and numerical technique used here will be detailed followed by a detailed discussion on the numerical results, including a qualitative comparison with previously published two-dimensional results.

2. Theory and Numerical Method

In this study, the electroosmotically driven flow through a slit microchannel (i.e., a channel formed between two parallel plates) exhibiting one of the three periodically repeating heterogeneous surface patterns shown in Figure 1 is considered. The first two of these patterns, Figure 1, parts a and b, are in essence one-dimensional surface patterns and are only considered here in order to provide a validation of the results via a qualitative comparison with the aforementioned studies of Ajdari[20] and Stroock et al.[25] Since the pattern is repeating, the computational domain is reduced to that over a single periodic cell, demonstrated by the dashed lines in Figure 1. Note that this periodic boundary condition ignores any entrance/exit effects and thus is not valid for the first and last periodic units on the surface. To further minimize the size of the solution domain, it has been assumed that the heterogeneous surface pattern is symmetric about the channel midplane, resulting in the computational domain shown in Figure 2. As a result of these two simplifications, the inflow and outflow boundary surfaces 2 and 4 (as are labeled in Figure 2 and as will be referred symbolically by the symbol Γ in the following discussion) represent periodic boundaries on the computational domain, while surface 3 at the channel midplane represents a symmetry boundary. From Figure 1 it can be seen that in all cases the surface pattern is symmetric about Γ_5 and Γ_6, and thus these surfaces also represent symmetry boundaries. Further

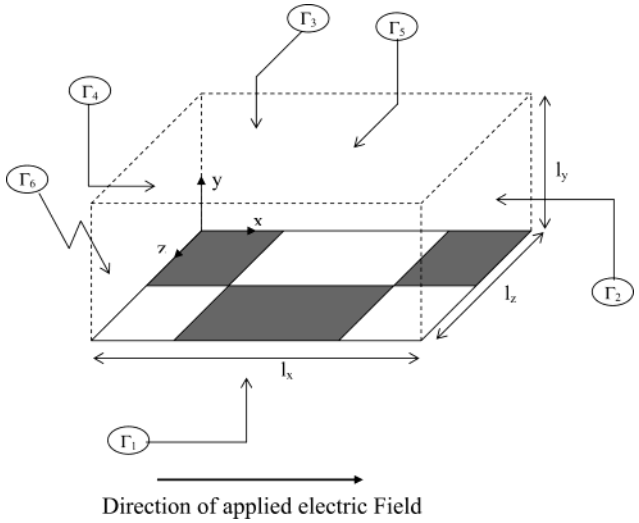

Figure 2. Domain for periodically repeating computational cell showing location of computational boundaries.

details regarding periodicity as related to this study are provided throughout this section. For a general discussion however the reader is referred to a paper by Patankar et al.[31]

2.1. Analytical Model. As mentioned above, electroosmotic flow occurs when an applied driving voltage interacts with the charge in the electrical double layer near the surface, resulting in a local net body force that tends to induce bulk fluid motion. To model the flow through this periodic unit, we require a description of the ionic species distribution, the double-layer potential, the flow field, and the applied potential. To begin, the divergence of the ion species flux (here we consider a monovalent, symmetric electrolyte as our model species), often referred to as the Nernst−Planck conservation equations, is used to describe the positive and negative ion densities (given below in nondimensional form).

$$\tilde{\nabla}\cdot(-\tilde{\nabla}N^+ - N^+\tilde{\nabla}\Phi + Pe^+N^+\mathbf{V}) = 0 \qquad (1a)$$

$$\tilde{\nabla}\cdot(-\tilde{\nabla}N^- + N^-\tilde{\nabla}\Phi + Pe^-N^-\mathbf{V}) = 0 \qquad (1b)$$

where N^+ and N^- are the nondimensional positive and negative species concentrations ($N^+ = n^+/n_o$, $N^- = n^-/n_o$, where n_o is the bulk ionic concentration), Φ is the nondimensional electric field strength ($\Phi = e\phi/k_bT$, where e the elemental charge, k_b is the Boltzmann constant, and T is the temperature in Kelvin), $\mathbf{V}$ is the nondimensional velocity ($\mathbf{V} = \mathbf{v}/v_o$ where v_o is a reference velocity), and the $\sim$ sign signifies that the gradient operator has been nondimensionalized with respect to the channel half-height (l_y in Figure 1). The two species Peclet numbers are given by $Pe^+ = v_o l_y/D^+$ and $Pe^- = v_o l_y/D^-$, where D^+ and D^- are the diffusion coefficients for the positive and negative species, respectively.

Along the heterogeneous surface (Γ_1 in Figure 2) and symmetry boundaries of the computational domain (Γ_3, Γ_5, and Γ_6), zero flux boundary conditions are applied to both eq 1a and eq 1b; see Erickson and Li[19] for explicit equations. As mentioned earlier, along faces Γ_2 and Γ_4, periodic conditions are applied which take the form shown below.

$$N_2^+ = N_4^+ \qquad \text{on } \Gamma_2, \Gamma_4 \qquad (1c)$$

$$N_2^- = N_4^- \qquad \text{on } \Gamma_2, \Gamma_4 \qquad (1d)$$

The velocity field is described by the Navier−Stokes equations for momentum, modified to account for the electrokinetic

body force, and the continuity equation as shown below.

$$Re(\mathbf{V}\cdot\tilde{\nabla}\mathbf{V}) = -\tilde{\nabla}P + \tilde{\nabla}^2\mathbf{V} - F(N^+ - N^-)\tilde{\nabla}\Phi \quad (2a)$$

$$\tilde{\nabla}\cdot\mathbf{V} = 0 \quad (2b)$$

where F is a nondimensional constant ($F = n_o l_y k_b T/\mu v_o$), which accounts for the electrokinetic body force, Re is the Reynolds number ($Re = \rho v_o l_y/\mu$, where ρ is the fluid density and μ is the viscosity), and P is the nondimensional pressure. Along the heterogeneous surface, Γ_1, a no slip boundary condition is applied. At the upper symmetry surface, Γ_3, we enforce a zero penetration condition for the y-component of velocity and zero gradient conditions for the x and z terms, respectively. Similarly a zero penetration condition for the z-component of velocity is applied along Γ_5 and Γ_6, while zero gradient conditions are enforced for the x and y components. As with the Nernst−Planck equations, periodic boundary conditions are applied along Γ_2 and Γ_4.

For the potential field, we choose to separate, without loss of generality, the total nondimensional electric field strength, Φ, into two components.

$$\Phi(X,Y,Z) = \Psi(X,Y,Z) + E(X) \quad (3)$$

where the first component, $\Psi(X,Y,Z)$, describes the electrical double-layer field and the second component, $E(X)$, represents the applied electric field. In pressure-driven flows, $E(X)$ is the flow-induced streaming potential[19] and is generally quite weak. In this case however the gradient of $E(X)$ is of magnitude similar to the gradient of $\Psi(X,Y,Z)$ and thus cannot be decoupled to simplify the solution to the Poisson equation. As a result for this case the Poisson equation has the form shown below.

$$\tilde{\nabla}^2\Psi + d^2E/dX^2 + K^2(N^+ - N^-) = 0 \quad (4a)$$

where K is the nondimensional double-layer thickness ($K^2 = \kappa^2 l_y^2/2$, where $\kappa = (2n_o e^2/\epsilon_w k_b T)^{1/2}$ is the Debye−Huckel parameter, the inverse of which is commonly referred to as the double-layer thickness). Two boundary conditions commonly applied along the solid surface for the above equation are either an enforced potential gradient proportional to the surface charge density or a fixed potential condition equivalent to the surface ζ-potential. In this case we choose the former, resulting in the following boundary condition applied along the heterogeneous surface.

$$\partial\Psi/\partial Y = -\Theta(X,Z) \qquad \text{on } \Gamma_1 \quad (4b)$$

where Θ is the nondimensional surface charge density ($\Theta = \sigma l_y e/\epsilon_w k_b T$, where σ is the surface charge density). Along the upper and side boundaries of the computational domain, Γ_3, Γ_5, and Γ_6, symmetry conditions are applied while periodic conditions are again applied at the inlet and outlet, Γ_2 and Γ_4.

To determine the applied electric field, $E(X)$, we enforce a constant current condition at each cross section along the x-axis as shown in eq 5a.

$$J_{const} = \int_0^{Z_{max}}\int_0^{Y_{max}}[J^+(X,Y,Z) - J^-(X,Y,Z)]\cdot n_x \, dY \, dZ \quad (5a)$$

where n_x in the above is a normal vector in the x direction and J^+ and J^- are the nondimensional positive and negative current densities. Assuming monovalent ions for both positive and negative species (as was discussed earlier) and substituting in the ionic species flux terms (i.e., those contained within the outer set of brackets) from eq 1a and eq 1b into J^+ and J^- (note that the flux terms in eq 1b must be multiplied by Pe^+/Pe^- so that all components are scaled by the same diffusion coefficient), condition 5a reduces to the following.

$$J_{const} = \int_0^{Z_{max}}\int_0^{Y_{max}}\left(-\left[\frac{\partial N^+}{\partial X} - \frac{Pe^+}{Pe^-}\frac{\partial N^-}{\partial X}\right] - \left[N^+ + \frac{Pe^+}{Pe^-}N^-\right]\frac{\partial(\Psi + E)}{\partial X} + [Pe^+(N^+ - N^-)V_x]\right)dY\,dZ \quad (5b)$$

which is a balance between the conduction (term 2) and convection (term 3) currents with an additional term to account for any induced current due to concentration gradients. Solving eq 5a for the applied potential gradient yields the final form of condition 5a given below.

$$\frac{dE}{dX} = \left\{\int_0^{Z_{max}}\int_0^{Y_{max}}\left(-\left[\frac{\partial N^+}{\partial X} - \frac{Pe^+}{Pe^-}\frac{\partial N^-}{\partial X}\right] - \left[N^+ + \frac{Pe^+}{Pe^-}N^-\right]\frac{\partial\Psi}{\partial X} + [Pe^+(N^+ - N^-)V_x]\right)dY\,dZ - J_{const}\right\}\Bigg/ \left[\int_0^{Z_{max}}\int_0^{Y_{max}}\left(N^+ + \frac{Pe^+}{Pe^-}N^-\right)dY\,dZ\right] \quad (5c)$$

The value of J_{const} in the above equations is governed by the average magnitude of the applied electric field gradient (referred to in subsequent text and figures by the symbol V_{app}) over the periodic unit (note that this is different from dE/dX, which represents the local potential field gradient). The value of J_{const} for each value of the applied electric field is computed from eq 5b by assuming homogeneous surface properties and substituting V_{app} for dE/dX (since in this case the two are equivalent).

2.2. Numerical Method and Solution Algorithm. The above system of equations was solved with the finite element method[32] using the in-house written BLOCS (bio-lab-on-a-chip simulation) code. Here we provide some brief details on the numerical method concentrating on the implementation of this code to this application. For further details (including comments on general verification of the code and computational expense) the reader is referred to Erickson and Li.[19] To begin, the computational domain was discretized using 27-noded three-dimensional elements, which were refined within the double-layer region near the surface and further refined in locations where discontinuities in the surface charge density were present. Triquadratic basis functions were used for all the unknowns N^+, N^-, V_x, V_y, V_z, and Ψ. In general the use of these higher order elements and basis functions (as opposed to eight-noded trilinear elements) was found to be optimal, as they could better approximate the sharp gradients in velocity, species concentration, and electric potential within the double-layer region. In all cases periodic conditions were imposed using the technique described by Sáez and Carbonell.[33]

The solution algorithm began by forming the computational mesh and performing the elemental matrix integrations. All solution variables were then set to zero with the exception of N^+, N^-, and Ψ, which were initially approximated with a classical Poisson−Boltzmann distribution.[34,35] Using these as initial guesses a semiimplicit, Newtonian iteration technique was used to solve eqs 1a, 1b, and 4a simultaneously. In general it was found that the convergence could only be achieved when the double-layer potentials, Ψ, in the nonlinear terms of eqs 1a and 1b were fully implicit to the solution and the N^+ and N^- terms explicit. Once convergence of all three variables was obtained, the forcing term in the Navier−Stokes equations could

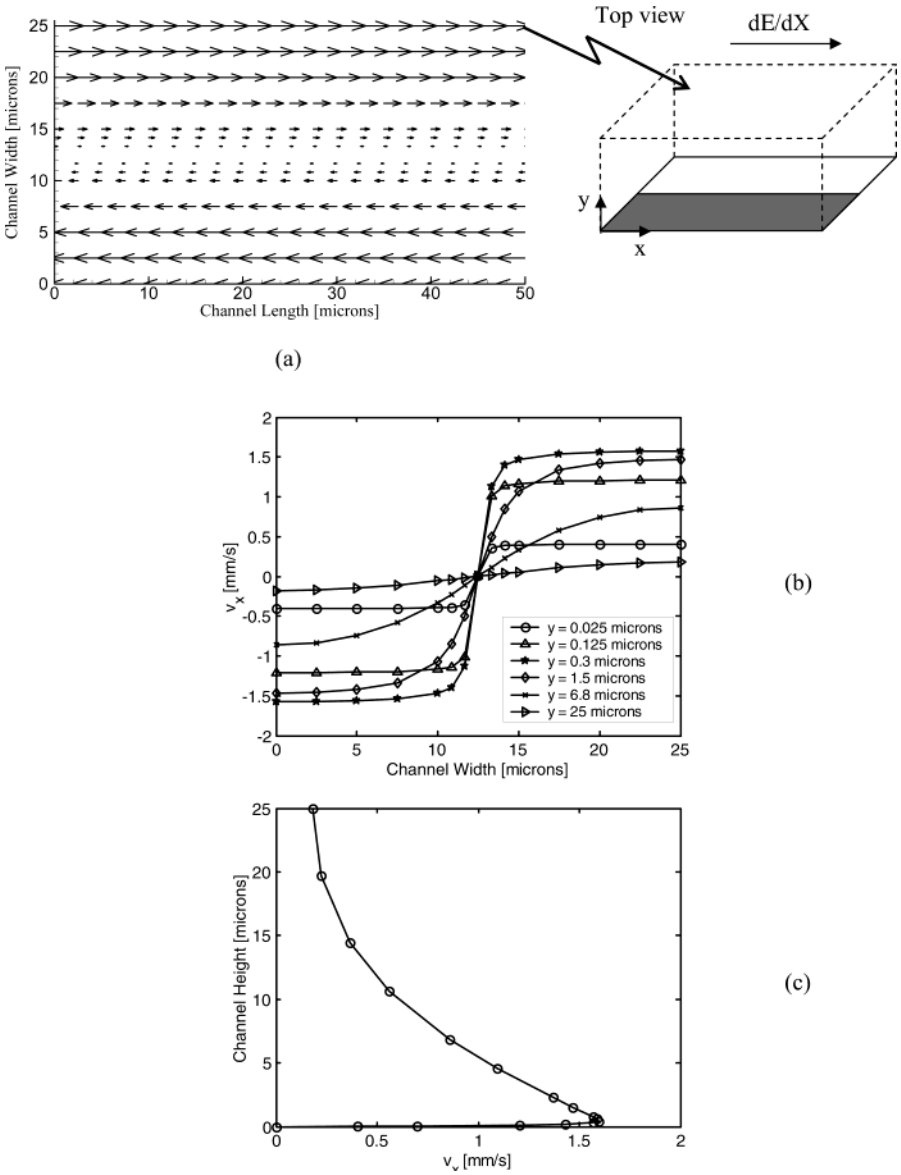

Figure 3. Electroosmotic flow over a lengthwise heterogeneous surface pattern with $\sigma_{homo} = -4 \times 10^{-4}$ C/m^2 and $\sigma_{hetero} = +4 \times 10^{-4}$ C/m^2 in a 1×10^{-5} M ($1/\kappa = 0.1$ μm) monovalent electrolyte: (a) velocity vectors at symmetry plane, $y = 25$ μm; (b) flow magnitude at various locations along the channel height; (c) velocity profile along Γ_5 ($l_z = 25$ μm) plane.

be evaluated and eqs 2a and 2b were solved concurrently using a penalty method.[32] Following convergence of the flow solution, eq 5c was evaluated at each cross section to yield updated values of $E(X)$. The above process was repeated until convergence of $E(X)$ was obtained.

3. Results and Discussion

3.1. Comparison with Previously Published Results. To ensure the accuracy of the solutions presented below, a large amount of model verification was performed. Results from the three-dimensional model were verified against the well-known classical results for homogeneous surfaces[34,35] as well as the one-dimensional experimental results presented by Herr et al.[27] In addition, the BLOCS code used in this study has been checked against several classical flow test problems, such as flow over a backward step and flow in a square cavity, and experimentally verified in previous works.[36]

Of immediate interest here would be a qualitative comparison with the two-dimensional results of Ajdari[20] and Stroock et al.[25] using the lengthwise and crosswise strip patterns as shown in Figure 1a,b (note that Ajdari actually considered a sinusoidally varying surface charge density as opposed to the step changes examined here; however, as will be shown, a similar flow structure exists). To do this, we consider a computational domain with dimensions $l_x = 50$ μm, $l_y = l_z = 25$ μm (the $x-y-z$ coordinate system is as shown in Figure 2) containing a 1×10^{-5} M KCl solution (thus a double-layer thickness, $1/\kappa$, of 0.1 μm) and an applied driving voltage of 500 V/cm. All simulations were conducted for liquid properties at 25 °C ($\mu = 1.003 \times 10^{-3}$ kg/ms, $\rho = 998$ kg/m^3, $\epsilon_w = 7.1009 \times 10^{-10}$ C^2/Nm^2). Chemical properties of K^+ and Cl^- ions were taken from Vanysek[37] ($D_K = 1.957 \times 10^{-5}$ cm^2/s, $D_{Cl} = 2.032 \times 10^{-5}$ cm^2/s). In each case a homogeneous surface charge density of $\sigma_{homo} = -4 \times 10^{-4}$ C/m^2 and heterogeneous patches with $\sigma_{hetero} = +4 \times 10^{-4}$ C/m^2 (corresponding to ζ-potentials of approximately -50 and $+50$ mV, respectively) are considered, which results in an excess of positive ions over the homogeneous region and negative ions over the heterogeneous region. The results for the lengthwise strips are shown in Figure 3 and Figure 4 for the crosswise strips.

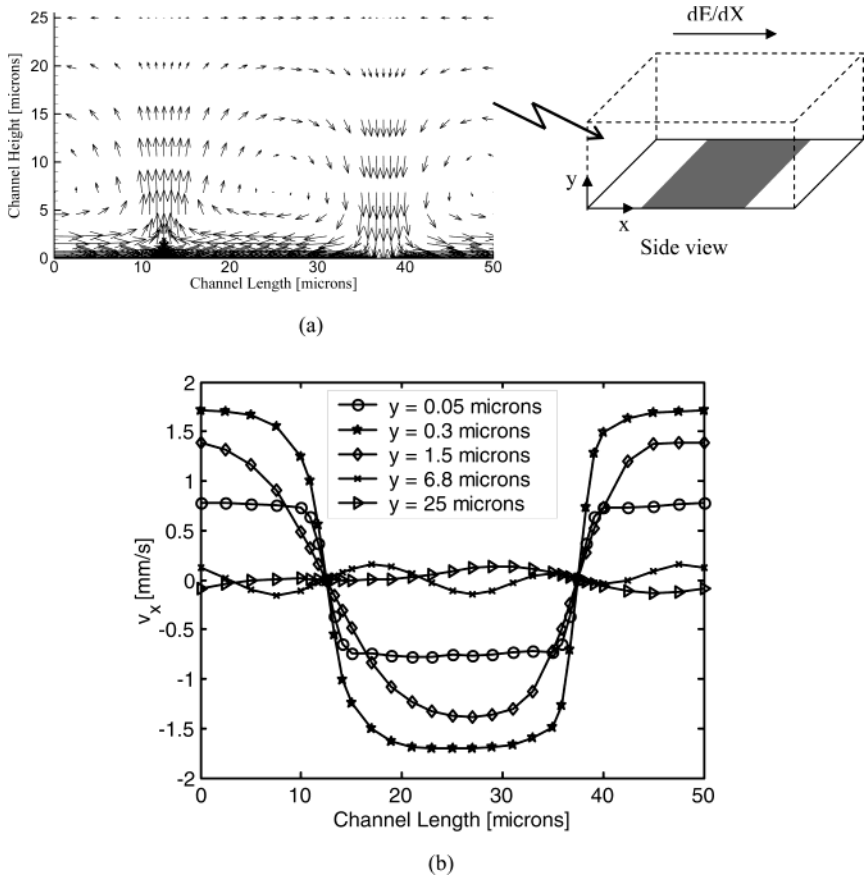

Figure 4. Electroosmotic flow over a crosswise heterogeneous surface pattern with $\sigma_{homo} = -4 \times 10^{-4}$ C/m^2 and $\sigma_{hetero} = +4 \times 10^{-4}$ C/m^2 in a 1×10^{-5} M monovalent electrolyte ($1/\kappa = 0.1$ μm): (a) side view of velocity vectors in $x-y$ plane; (b) magnitude of x direction velocity at various locations along the channel height.

Figure 3a shows a top view of the velocity vectors at the symmetry plane (Γ_3, $l_y = 25$ μm). As was observed by Stroock et al.,[25] the flow is directed along the negative x-axis over the heterogeneous strips and the positive x-axis over the homogeneous patch, in both cases becoming weaker and approaching zero near the transition point. Also of interest is the change in the magnitude of the induced flow velocity with increasing distance from the surface. As can be seen in Figure 3b,c, the velocity reaches a maximum at a distance of approximately $3/\kappa$ from the surface (which is approximately equivalent to the edge of the double layer, where the net charge density is essentially zero) and then becomes lower and lower as the distance from the double layer increases. From Figure 3b it is also apparent that the velocity profile changes from a near step change within the double layer, where the electroosmotic force is strongest, to a significantly more curved and flatter profile as the distance from the surface becomes greater and viscous forces begin to dominate. Extrapolating from these results, one would expect the flow, in a very large channel, to eventually reach a near stagnant flow at the midplane, which was an observation originally made by Ajdari[20] for the sinusoidal varying surface pattern.

As is shown by the velocity vectors in Figure 4a, the presence of crosswise heterogeneous strips results in a series of alternating clockwise and counterclockwise tumbling regions, or regions of flow circulation whose center axis is perpendicular to the direction of the applied electric field. An analogous effect was predicted by Ajdari[20] for the sinusoidal surface pattern and observed experimentally by Stroock et al.[25] for a similar strip pattern, lending further credibility to the proposed model. Figure 4b shows the magnitude of the x-direction velocity at increasing distances from the surface. Similar to the previous case, a near step change in v_x is observed at the discontinuity in surface charge density within the double layer and the maximum velocity is obtained at a distance of $3/\kappa$ from the surface. At further distances from the surface, viscous forces begin to dominate and momentum diffusion tends to broaden this step change while reducing the magnitude of the velocity, eventually resulting in the sinusoidal-type pattern above the circulation axis at the symmetry plane ($y = 25$ μm).

3.2. Three-Dimensional Flow Structure for Patchwise Heterogeneous Surfaces. In the previous section we limited ourselves to the one-dimensional surface patterns shown in Figure 1a,b in order to provide some qualitative comparison of our proposed numerical model with the results of previous studies and to explore in greater detail some of the flow structure associated with these patterns. Here we extend this to consider the two-dimensional patchwise surface pattern shown in Figure 1c and to provide the first insights into the resulting three-dimensional flow structure. To do this, we again consider an $l_x = 50$ μm, $l_y = l_z = 25$ μm computational domain (see Figure 2) containing a 10^{-5} M KCl solution, an applied driving voltage of 500 V/cm, and a $\sigma_{homo} = -4 \times 10^{-4}$ C/m^2. The simulations revealed three distinct flow patterns, depending on the degree of surface heterogeneity, each of which is shown in Figure 5. The contours in these figures represent the magnitude of the velocity perpendicular to the direction of the applied electric field ($v^2 = v_y^2 + v_z^2$) scaled by the maximum velocity in a homogeneous channel, which in this case is 1.7 mm/s.

At low degrees of surface heterogeneity ($\sigma_{hetero} \leq -2 \times 10^{-4}$ C/m^2) the streamline pattern shown in Figure 5a was obtained. As can be seen, a net counterclockwise flow perpendicular to

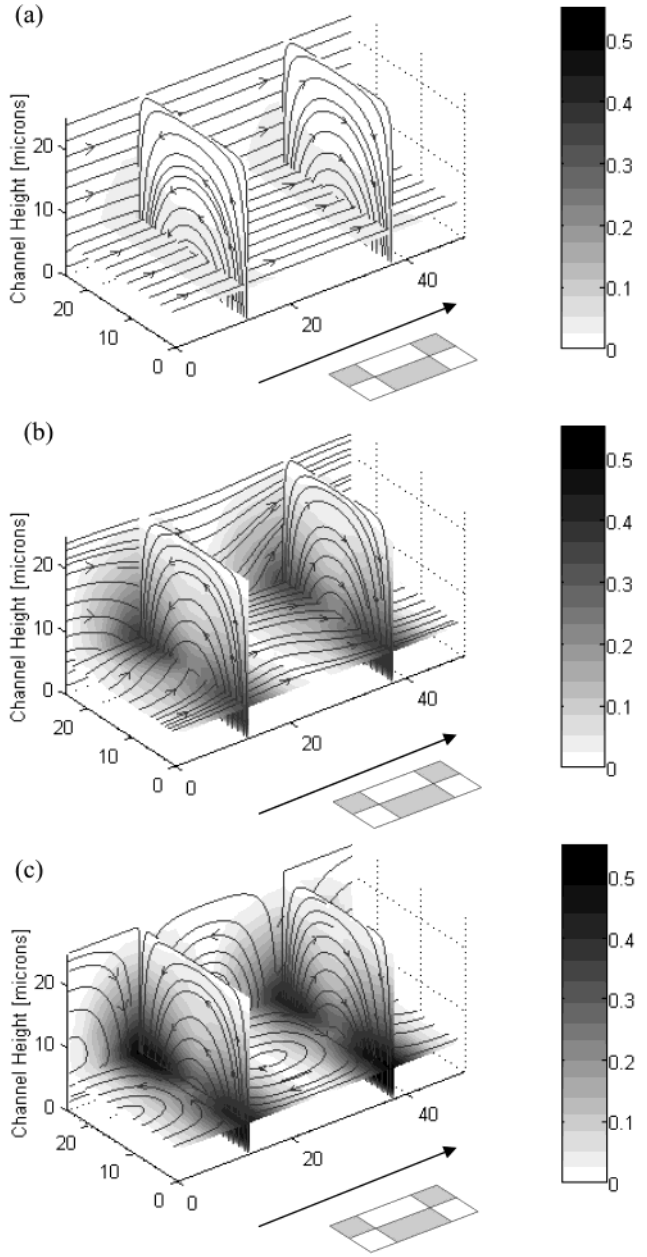

Figure 5. Electroosmotic flow streamlines over a patchwise heterogeneous surface pattern with $\sigma_{homo} = -4 \times 10^{-4}$ C/m^2 and (a) $\sigma_{hetero} = -2 \times 10^{-4}$ C/m^2; (b) $\sigma_{hetero} = +2 \times 10^{-4}$ C/m^2; (c) $\sigma_{hetero} = +4 \times 10^{-4}$ C/m^2. Contours represent the magnitude of velocity perpendicular to the applied potential field, scaled by the maximum velocity in a homogeneous channel. Arrow represents direction of applied electric field.

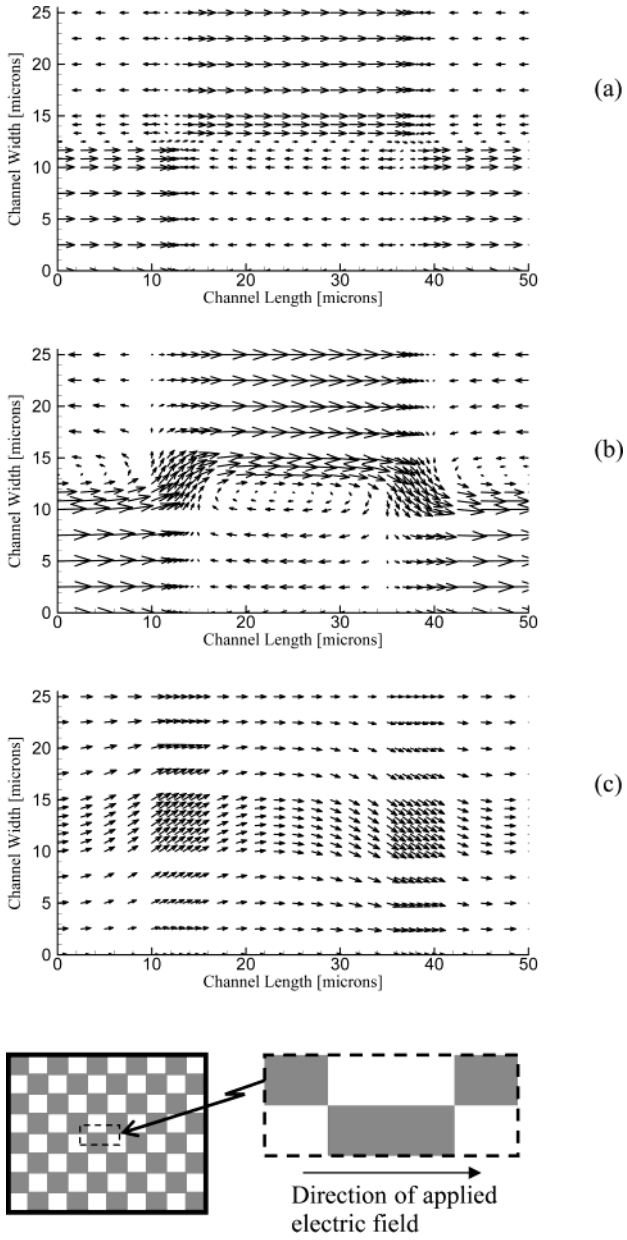

Figure 6. Velocity vectors in the $x-z$ plane over a patchwise heterogeneous surface pattern with $\sigma_{homo} = -4 \times 10^{-4}$ C/m^2 and $\sigma_{hetero} = +2 \times 10^{-4}$ C/m^2 at distances of (a) 0.05 μm, (b) 1.5 μm, and (c) 10.5 μm above the surface.

the applied electric field is present at the first transition plane (i.e., at the initial discontinuity in the heterogeneous surface pattern) and a clockwise flow at the second transition plane. This flow circulation is a pressure-induced effect that arises as a result of the transition from the higher local fluid velocity (particularly in the double layer) over the homogeneous surface on the right-hand side at the entrance, to the left-hand side after the first transition plane (and vice versa at the second transition plane). To satisfy continuity, then there must be a net flow from right to left at this point, which in this case takes the form of the circulation discussed above. The relatively straight streamlines parallel with the applied electric field indicate that at this level the heterogeneity is too weak to significantly disrupt the main flow.

While a similar circulation pattern at the transition planes was observed as the degree of surface heterogeneity was increased into the intermediate range (-2×10^{-4} C/m$^2 \le \sigma_{hetero} \le +2 \times 10^{-4}$ C/m^2), it is apparent from the darker contours shown in Figure 5b that the strength of the flow perpendicular to the applied electric field is significantly stronger, reaching nearly 50% of the velocity in the homogeneous channel. Unlike in the previous case, it is now apparent that the streamlines parallel with the applied electric field are significantly distorted due to the much slower or even oppositely directed velocity over the heterogeneous patch. Figure 6 shows the evolution of the flow pattern for this case with increasing distance from the surface. As was noted in section 3.1 with respect to the lengthwise strip pattern, the flow patterns parallel with the surface tend to degrade as the distance from the double-layer region increases. This effect is again visible here, as a clear circulation pattern can be observed very near the surface with the flow in the opposite direction to the applied electric field

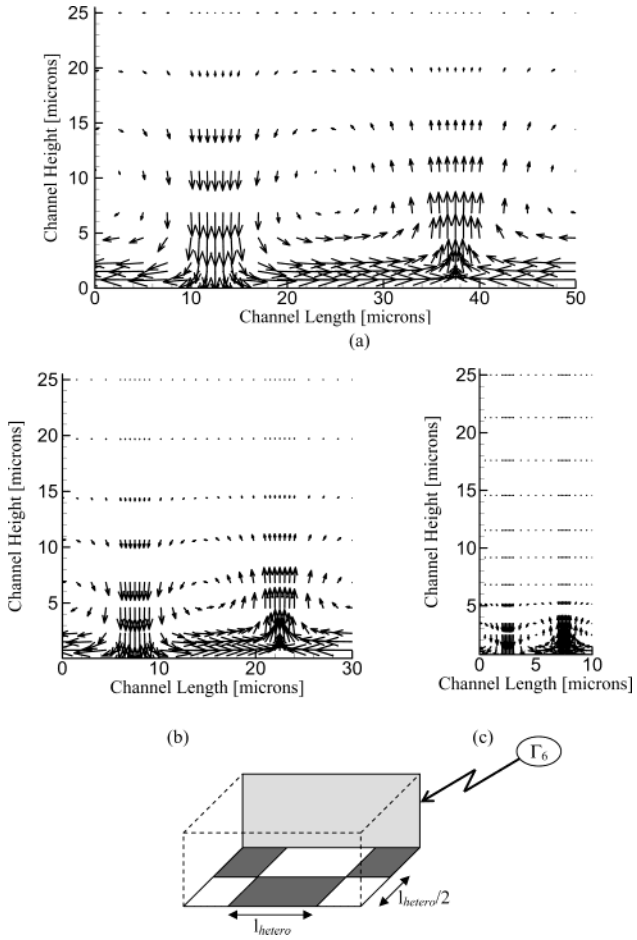

Figure 7. Influence of heterogeneous patch size on velocity vectors in the Γ_6 plane over a patchwise heterogeneous surface pattern with $\sigma_{homo} = -4 \times 10^{-4}$ C/m^2 and $\sigma_{hetero} = +4 \times 10^{-4}$ C/m^2: (a) $l_{hetero} = 25$ μm; (b) $l_{hetero} = 15$ μm; and (c) $l_{hetero} = 5$ μm.

over the heterogeneous patch, Figure 6a. As the distance from the surface is increased, the circulation becomes stronger, reaching a maximum near the edge of the double-layer region, Figure 6b. Farther out from the surface, Figure 6c, the circulation pattern is lost, leaving a more uniform flow field with only a slightly disturbed velocity over the heterogeneous regions.

At even higher degrees of heterogeneity ($+2 \times 10^{-4}$ C/m^2 $\leq \sigma_{hetero} \leq +4 \times 10^{-4}$ C/m^2) a third flow structure is observed in which a dominant circulatory flow pattern exists along all three coordinate axes, as shown in Figure 6c. This results in a negligible, or even nonexistent, bulk flow in the direction of the applied electric field (which is to be expected since the average surface charge density for these cases is very near zero). As indicated by the contour plots, the velocity perpendicular to the flow axis has again increased in magnitude, reaching a maximum at the edge of the double layer near the symmetry planes at the location where a step change in the surface charge density has been imposed.

3.3. Influence of Patch Size on the Penetration Depth of the Flow Disturbance. As electroosmotically driven flow is an inherently surface driven effect, it is of significant practical interest (in mixing applications for example) to examine how deeply the circulation patterns observed above will penetrate into the bulk flow. We have already shown in Figure 6 that the near-surface flow structure tends to degrade as the distance from the double layer becomes greater, and we now seek to better quantify this effect in terms of the size of the heterogeneous patches and the channel height. In Figure 7 the velocity vectors along the Γ_6 plane are shown for the case of oppositely charged patches (as in the case shown in Figure 5c) with sizes ranging from 25 μm by 25 μm square to 5 μm by 5 μm square. For all cases a 25 μm channel half-height (l_y) is maintained; however the length (l_x) and width (l_z) of the computational cell were appropriately adjusted as the patch size was changed. From these figures two interesting effects can be observed. First it can be seen that as the size of the heterogeneity is decreased, the flow disturbance is confined to a thinner region near the wall, leaving a near-stagnant flow in the center of the channel (as one would expect since the average surface charge density is zero). In general it was observed that for the oppositely charged case the penetration depth of the flow disturbance is approximately equivalent to the size of the heterogeneous patch. It was also observed (not shown) that as the degree of heterogeneity was decreased, so was the penetration depth, and thus the oppositely charged case shown in Figure 7 represents a maximum. Second it is also apparent from the size of the vectors that as the heterogeneous patch size is decreased, so is the magnitude of the flow disturbance. The coupling of these two effects suggests that significant flow disturbance is likely to be observed only when the heterogeneous patch size is of the same order of magnitude as the channel height.

3.4. Influence of Applied Electric Field and Bulk Concentration on the Flow Structure. It is well known that the velocity of an electroosmotic flow is linearly proportional to the magnitude of the applied electric field (as can be deduced from eq 2a). The fluid velocity in the flow patterns shown above obeys the identical scaling laws. Similarly, proportionally increasing the magnitude of σ_{homo} and σ_{hetero} increased the magnitude of the flow circulation but had no effect on the overall flow structure. As a result, the flow structures shown in the preceding figures are quite general and are not significantly affected by either of these quantities.

Further simulations revealed that, for the cases examined here where the thickness of the double layer is significantly less than the channel height and the heterogeneous patch size, the double-layer thickness (or equivalently the bulk ionic concentration, n_o) had only a minor effect on the flow field. For thicker double layers (for example $n_o = 10^{-6}$ M, $1/\kappa = 1$ μm) a slight reduction in the magnitude of the flow field was observed (at equivalent surface potentials), as induced pressure effects began to influence the velocity field within the EDL; however the overall flow structure was not significantly altered.

3.5. Electrophoritic and Convective Effects on the Double-Layer Field. As alluded to earlier, the full Nernst−Planck−Poisson formulation used here (as opposed to the traditional Poisson−Boltzmann distribution) allows us to also examine how the electrophoritic influence of the applied electric field and the convective effects of the irregular flow structures will disturb the double-layer structure. Figure 8 shows the scaled net charge density $(n^+ - n^-)/n_o$ distribution along the Γ_6 face at increasing distances from the heterogeneous surface for the standard computational domain discussed above with $\sigma_{homo} = -4 \times 10^{-4}$ C/m^2 and $\sigma_{hetero} = +4 \times 10^{-4}$ C/m^2. From Figure 8a it is apparent that the near surface net charge density field becomes slightly distorted compared with the Poisson−Boltzmann distribution (which is represented by the $V_{app} = 0$ case) as the applied electric field is increased.

In an earlier work concerning pressure-driven flow over heterogeneous surfaces[19] it was observed that at Reynolds numbers greater than 10 and a bulk ionic strength less than 10^{-5} M, convective effects can significantly distort the double-layer field from the traditional Poisson−Boltzmann distribution. For

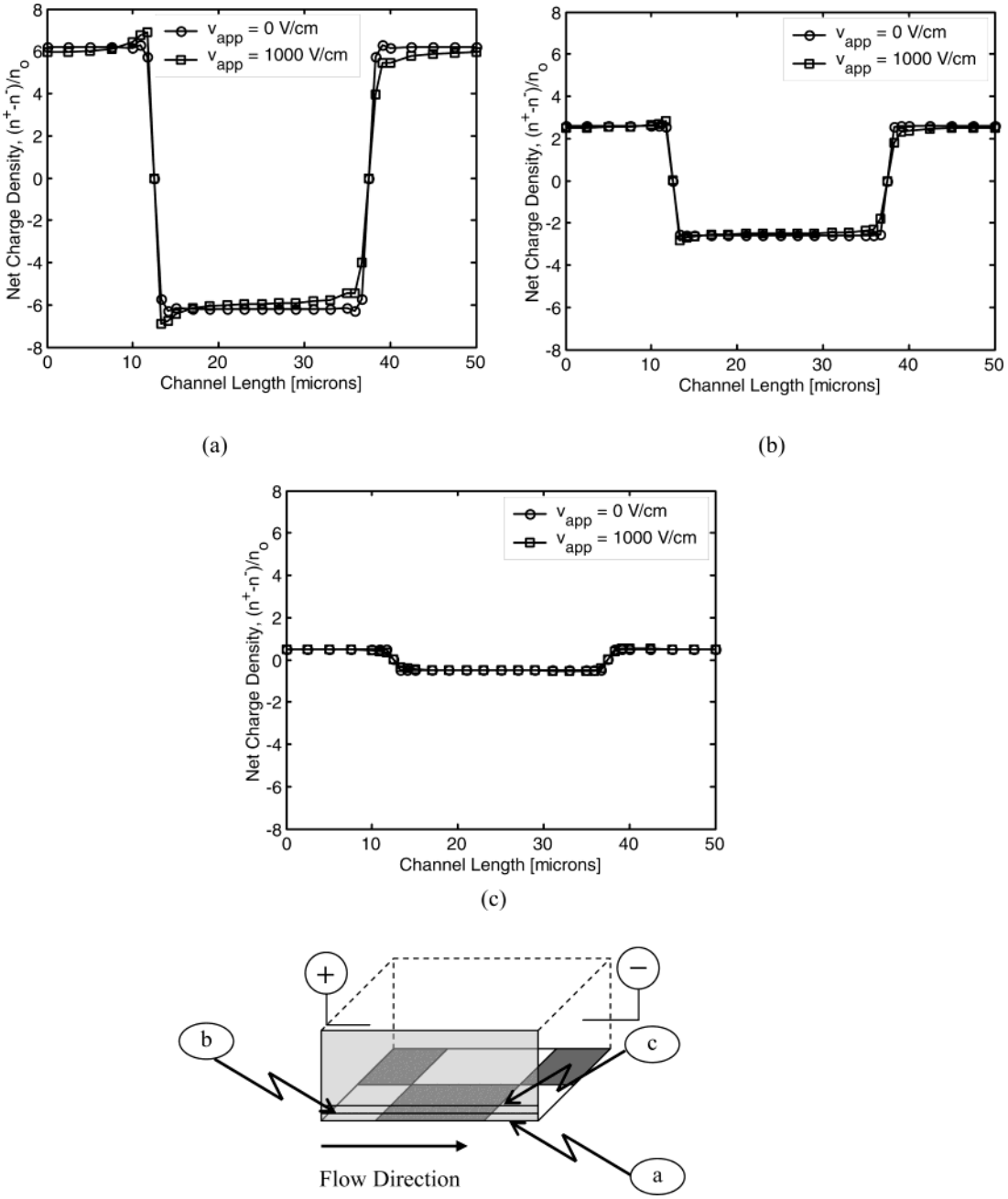

Figure 8. Influence of applied electric field on net charge density distribution in the double layer with $\sigma_{homo} = -4 \times 10^{-4}$ C/m^2, $\sigma_{hetero} = +1 \times 10^{-4}$ C/m^2 in a 1×10^{-5} M ($1/\kappa = 0.1$ μm) electrolyte: (a) $y = 0$ μm; (b) $y = 0.05$ μm; and (c) $y = 0.2$ μm.

the electroosmotic case examined here, the highest Reynolds number obtained was $Re = 0.09$ (corresponding to Pe^+ and Pe^- values of 0.02), and thus the convective terms in eqs 1a and 1b could not have significantly influenced the result. The cause of the disturbance observed here is the electrophoritic influence of the applied electric field (which is orders of magnitude stronger than the induced streaming potential in the pressure-driven case). In this case the applied field induces a net flux of positive ions from left to right and negative ions from right to left (see eqs 1a and 1b). As a result, an increase in the magnitude of the net charge density is observed near the first step change in surface potential as the ion flux from the left (where positive ions are in excess) meets the ion flux from the right (where negative ions are in excess). In contrast, at the second transition point a decrease in the net charge density is observed since in both cases the net ion flux is away from this point. As is apparent from Figure 8b,c however this effect is limited to the region very near the surface, as double-layer field is shown to resemble very closely a Poisson−Boltzmann distribution at distances of $0.5/\kappa$ and $2/\kappa$ from the surface. In general, this rearrangement of the net charge density field had only a small affect on the local fluid velocity, in that the calculated velocity was slightly higher in the regions where the net charge density was increased and vice versa. As was noted in section 3.4, however, this did not have a significant influence on the overall flow structure.

4. Summary and Conclusions

The potential benefits that electroosmotic flow has to offer as a primary method of species transport have made it the preferred choice of most lab-on-chip devices. Surface electrokinetic heterogeneity occurs in various lab-on-chip devices, for example, through biofouling (it is important to recognize that many types of biofouling would also result in an additional flow

impedance due to changes in the surface profile). Surface electrokinetic heterogeneity can be used (for example, to enhance mixing or reduce band broadening) in a variety of microfluidic applications. In this study the structure of electroosmotically driven flows over periodically repeating heterogeneous surfaces has been investigated using a numerical model based on a simultaneous solution to the coupled Nernst−Planck, Poisson, and Navier−Stokes equations.

The presence of periodically repeating heterogeneous patches is shown to induce one of three distinct flow structures depending on the relative difference between the surface charge density of the homogeneous and heterogeneous regions. Small differences in the charge density are shown to induce fluid motion perpendicular to the applied electric field; however the bulk flow remains largely unaffected. As the degree of heterogeneity is increased, the streamlines in the direction of the applied electric field become significantly distorted; however the effect is minimized as the distance from the surface is increased. When oppositely charged surfaces are encountered, a strong circulatory flow regime is observed in which flow perpendicular to the applied electric field is of the same order as that parallel with it and the net volume flow rate becomes negligible. It is also shown that the induced flow patterns are limited to a layer near the surface with a thickness equivalent to the length scale of the heterogeneous patch and that as the average size of the heterogeneous region decreases, the effect becomes smaller in magnitude and more localized. In addition it was demonstrated that while convective effects are small, the electrophoritic influence of the applied electric field could distort the net charge density field near the surface, resulting in a significant deviation from the traditional Poisson−Boltzmann double-layer distribution.

Acknowledgment. The authors are thankful for the financial support of the Natural Sciences and Engineering Research Council through a scholarship to D.E. and through a research grant to D.L.

References and Notes

(1) Jacobson, C. S.; Ramsey, J. M. *Anal. Chem.* **1997**, *69*, 3212.
(2) Ermakov, S. V.; Jacobson S. C.; Ramsey, J. M. *Anal. Chem.* **2000**, *72*, 3512.
(3) Griffiths, S. K.; Nilson, R. H. *Anal. Chem.* **2000**, *72*, 5473.
(4) Molho, J. I.; Herr A. E.; Mosier, B. P.; Santiago, J. G.; Kenny, T. W.; Brennen, R. A.; Gordon, G. B.; Mohommadi, B. *Anal. Chem.* **2001**, *73*, 1350.
(5) Dutta, B.; Leighton, D. T. *Anal. Chem.* **2002**, *74*, 1007.
(6) Johnson, T. J.; Ross, D.; Gaitan, M.; Locascio, L. E. *Anal. Chem.* **2001**, *73*, 3656.
(7) Hadd, A. G.; Raymond, D. E.; Halliwell, J. W.; Jacobson, S. C.; Ramsey, J. M. *Anal. Chem.* **1997**, 34077.
(8) Daridon, A.; Fascio. V.; Lichtenberg, J.; Wutrich, R.; Langen, H.; Verpoorte, E.; de Rooij, N. F. *Fresenius J. Anal. Chem.* **2001**, *371*, 261.
(9) Krishnan, M.; Namasivayam, V.; Lin, R.; Pal, R.; Burns, M. A. *Curr. Opin. Biotech.* **2001**, *12*, 92.
(10) Norde, W.; Rouwendal, E. *J. Colloid Interface Sci.* **1990**, *139*, 169.
(11) Elgersma, A. V.; Zsom, R. L. J.; Lyklema, J.; Norde, W. *Colloid Surf.* **1992**, *65*, 17.
(12) Zembala, M.; Déjardin, P. *Colloid Surf. B* **1994**, *3*, 119.
(13) Werner, C.; Jacobasch, H. J. *Macromol. Symp.* **1996**, *103*, 43.
(14) Fuerstenau, D. W. *J. Phys. Chem.* **1956**, *60*, 981.
(15) Hayes, R.; Böhmer, M.; Fokkink, L. *Langmuir* **1999**, *15*, 2865.
(16) Zembala, M.; Adamczyk, Z. *Langmuir* **2000**, *16*, 1593.
(17) Adamczyk, Z.; Warszynzki, P.; Zembala, M. *Bull. Polish Acad. Sci. Chem.* **1999**, *47*, 239.
(18) Hayes, R. *Colloids Surf. A* **1999**, *146*, 89.
(19) Erickson, D.; Li, D. *Langmuir* **2002**, *18*, 8949.
(20) Ajdari, A. *Phys. Rev. Lett.* **1995**, *75*, 755.
(21) Ajdari, A. *Phys. Rev. E* **1996**, *53*, 4996.
(22) Ajdari, A. *Phys. Rev. E* **2001**, *65*, 016301.
(23) Anderson, J. L. *J. Colloid Interface Sci.* **1985**, *105*, 45.
(24) Ghosal, S. *J. Fluid Mech.* **2002**, *459*, 103.
(25) Stroock, A. D.; Weck, M.; Chiu, D. T.; Huck, W. T. S.; Kenis, P. J. A.; Ismagilov, R. F.; Whitesides, G. M. *Phys. Rev. Lett.* **2000**, *84*, 3314.
(26) Long, D.; Stone, H.; Ajdari, A. *J. Colloid Interface Sci.* **1999**, *212*, 338.
(27) Herr, A.; Molho, J.; Santiago, J.; Mungal, M.; Kenny, T. *Anal. Chem.* **2000**, *72*, 1053.
(28) Keely, C.; van de Goor, T.; McManigill, D. *Anal. Chem.* **1994**, *66*, 4236.
(29) Johnson, T. J.; Ross, D.; Gaitan, M.; Locascio, L. E. *Anal.Chem.* **2001**, *73*, 3656.
(30) Erickson, D.; Li, D. *Langmuir* **2002**, *18*, 1883.
(31) Patankar, S.; Liu, C.; Sparrow, E. *J. Heat Trans.* **1977**, *99*, 180.
(32) Heinrich, J. C.; Pepper, D. W. *Intermediate Finite Element Method*; Taylor & Francis: London, 1999.
(33) Sáez. A.; Carbonell, R. *Int. J. Numer. Methods Fluids*. **1985**, *5*, 601.
(34) Lyklema, J. *Fundamentals of Interface and Colloid Science, Volume 1: Fundamentals*; Academic Press: New York, 1991.
(35) Lyklema, J. *Fundamentals of Interface and Colloid Science, Volume 2: Solid−Liquid Interfaces*; Academic Press: New York, 1995.
(36) Sinton, D.; Erickson, D.; Li, D. *J. Micromech. Microeng.* **2002**, *12*, 898.
(37) Vanysek, P. Ionic Conductivity and Diffusion at Infinite Dilution. In *CRC Handbook of Chemistry and Physics*, 3rd electronic edition; Lide, D. R., Ed.; CRC Press: Boca Raton, FL, 2000.